Nuclear Instruments and Methods in Physics Research A 693 (2012) 109–116

Contents lists available at SciVerse ScienceDirect

Nuclear Instruments and Methods in Physics Research A

journal homepage: www.elsevier.com/locate/nima

Photon flux and spectrum of γ-rays Compton sources

V. Petrillo [a,b,*], A. Bacci [a], R. Ben Alì Zinati [b], I. Chaikovska [e], C. Curatolo [a,b], M. Ferrario [c], C. Maroli [b], C. Ronsivalle [d], A.R. Rossi [a], L. Serafini [a], P. Tomassini [b], C. Vaccarezza [c], A. Variola [e]

[a] INFN Milano, Via Celoria, 16 20133 Milano, Italy
[b] Università degli Studi di Milano, Via Celoria, 16 20133 Milano, Italy
[c] LNF, INFN Via E.Fermi, 40 Frascati, Roma, Italy
[d] ENEA Via E.Fermi, 45 Frascati, Roma, Italy
[e] LAL Universite Paris-Sud IN2P3/CNRS, Orsay-Ville, France

ARTICLE INFO

Article history:
Received 25 May 2012
Received in revised form
7 July 2012
Accepted 9 July 2012
Available online 20 July 2012

Keywords:
Compton back scattering
γ Source

ABSTRACT

We analyze the characteristics of the γ radiation produced by Compton back-scattering of a high brightness electron beam produced by a photoinjector and accelerated in a linac up to energies of 360–720 MeV and a laser operated at about 500 nm, by comparing classical and quantum models and codes. The interaction produces γ rays in the range 4.9–18.8 MeV. In view of the application to nuclear resonance fluorescence a relative bandwidth of few 10^{-3} is needed. The bandwidth is reduced by taking advantage of the frequency–angular correlation typical of the phenomenon and selecting the radiation in an angle of tens of μrads. The foreseen spectral density is 20–6 photons per eV in a single shot, a number that can be increased by developing multi-bunch techniques and laser recirculation. In this way a final value of 10^4 photon per eV per second can be achieved.

1. Introduction

Many applications in physics require the availability of quasi-monochromatic X and γ radiation with large spectral intensity. Regarding X rays, one of their most important applications is the advanced imaging. New research techniques in the investigation of matter, which need a coherent illumination of the samples with a large flux of photons of high energy, permit in fact to reach spatial resolution of the order of the molecular and atomic scales and have been already used to probe nano-structured [1,2], inorganic [3,4] and organic [5,6] objects. Radiation at shorter wavelength, γ rays, is instead used to excite the nuclear resonant fluorescence (NRF), so that different nuclei can be identified by the distinct pattern of NRF emission peaks. Besides synchrotron radiation [7], free-electron lasers [8–11] and high-order harmonic generation in gases [12] Thomson and Compton sources are among the most performing devices producing radiation with short wavelength, high power, ultra-short time duration, large transverse coherence and tunability. Existing Thomson sources [13–17,35] have been already demonstrated to be an important tool for producing tunable quasi-monochromatic X/γ rays suitable for applications in advanced biomedical imaging and in many other fields such as crystallography, plasma, high energy, matter and nuclear physics. The Thomson source PlasmonX [18–20] is in the commissioning phase at the National Laboratory of Frascati (INFN-LNF). It is based on the back scattering of the light pulse of the high intensity Ti:sapphire laser FLAME [21] with the high brightness electron beam produced by the photoinjector SPARC [22]. SPARC actually delivers electron bunches of charge up to 1 nC, energy up to 170 MeV, and brightness larger than 10^{14} A/mrad^2. In its first application to Thomson sources, the photoinjector is foreseento operate currently at a final beam energy E of about 30 MeV, with the production of Doppler blue shifted hard X rays with a wavelength $\lambda_T \approx \lambda_0/(4\gamma^2)$ of fraction of 1 Å ($\lambda_0 = 800$ nm is the wavelength of FLAME and $\gamma \approx 60$), corresponding to photon energies $E_p = hc/\lambda_T$ (h is the Planck constant) of about 20 keV. The main application foreseen for this X beam at SPARC is mammography's imaging made with the phase contrast technique, while more energetic X pulses of 40–80 keV will permit to explore the fields of angiography and chest or skull radiography. Furthermore, the operations of PlasmonX will be extended, already at the present stage, to shorter wavelengths down to $\lambda \approx 10^{-12}$ m, by exploiting the electron beam, already transported in the linac and studied [10], at 150 MeV. Photons in this range of energy ($E_p \sim 500$ keV) can be used to test nuclear transitions of atoms. In the future, with the linac upgrade, electron beams up to 250 MeV will be accelerated, allowing the production of X rays with energies exceeding 1 MeV.

Within the framework of the ELI-NP (Extreme Light Infrastructure-Nuclear Physics) project, a γ-rays source, whose main

* Corresponding author at: INFN Milano, Via Celoria, 16 20133 Milano, Italy.
E-mail address: Petrillo@mi.infn.it (V. Petrillo).

0168-9002/$ - see front matter © 2012 Elsevier B.V. All rights reserved.
http://dx.doi.org/10.1016/j.nima.2012.07.015

applications are in the nuclear physics, is foreseen. Possible working points for the electrons could be at 360 and 720 MeV [23]. Operating, for instance, with the second harmonics of a laser, i.e. with $\lambda_0 = 523.5$ nm, photons of wavelengths shorter than 10^{-13} m, with energies up to 20 MeV, could be produced. The relative bandwidth required for many applications in nuclear physics is of order 10^{-3} with a maximized spectral photon density, as also stated in similar projects [24]. The characterization of such γ source is the first step of the development of a $\gamma-$e collider, where the same electron beam undergoes scattering with the γ rays produced in the first interaction with the laser. The most important quality factors that characterize Thomson/Compton sources, in addition to frequency, are total energy, spectral width and divergence of the X/γ radiation yield. All these quantities can be evaluated knowing coordinates and momenta of the electrons of the interacting beam together with the most important parameters of the laser pulse by means of a standard classical electrodynamic calculation [25], which gives the emitted power in the far field zone in both linear and nonlinear regime. Quantum effects coming from the recoil of the electron in the scattering with the laser photon have, however, to be evaluated and eventually taken into account [15,17,26,27] when the electron energy is large. These effects lead to a red shift of the source wavelength and their importance for a head to head impact can be estimated by weighting the magnitude of the factor $\Delta = 2(\lambda_p - \lambda_T)/(\lambda_p + \lambda_T)$, where $\lambda_T = \lambda_0(1-\beta)/(1+\beta) \approx \lambda_0/(4\gamma^2)$ is the Doppler red shifted wavelength of the photon scattered as given in the Thomson model for head on scattering, while $\lambda_p = \lambda_T + h/\gamma m_0 c$ is the photon wavelength in the Compton model, β being the modulus of the normalized speed of the electron, m_0 its rest mass and h the Plank constant. For the 150 MeV beam, $\Delta = 10^{-3}$, while in the case of the source at 360 MeV, Δ turns out to be slightly larger than 10^{-2}, a value at which recoil effects begin to become important and have to be embedded into the model. At larger energies the quantum effects cannot be disregarded. The first attempt to give a quantum-dynamical treatment of Compton interactions dates back to Klein and Nishina [28], who calculate the cross-section of the scattering in the electron reference frame by solving the Dirac equation in the presence of a semi-classical e.m. potential. In our case, the output X/γ rays has to be evaluated in the laboratory frame, and is the effect of the interaction of all electrons of the beam and photons of the laser pulse. In this paper, we will briefly recall the Thomson model, describing the numerical code TSST used when the quantum recoil is negligible. Then, we will go through the Compton cross-section evaluation for the electron–photon interaction, using a generic geometry in the laboratory frame, and following the field theory [29,30]. We will extend the calculation to an ensemble of electrons and photons, using realistic particle and laser beams. We will compare the spectra produced in this way with purely classical nonlinear calculations, based on the electrodynamic assumptions, and with the results of the Monte-Carlo code CAIN [31,32]. We will apply the codes to the case of ELI, providing the X/γ rays spectrum and spectral density, concluding with an optimized setup. Useful scaling laws for the total photon number, for the bandwidth and for the spectral density are presented and validated. Finally, we will give comments and conclusions.

2. Classical Thomson model

2.1. Thomson cross-section and TSST code

The classical model describing the interaction between electron and radiation, based on the fundamental laws of electromagnetism [25], has been widely analyzed in the framework of the development of Thomson sources [33,34,19,20] and already cross checked vs experiments [13,35].

When the interaction takes place between laser pulses few picosecond long in the linear or moderately nonlinear regime and ultrarelativistic electron bunches, the total scattered radiation intensity can be evaluated as sum of the distributions produced by the single particles.

The i-th electron, while entering the laser pulse, experiences longitudinal and transverse ponderomotive forces that respectively lower its longitudinal momentum and induce quivering and secular transverse motion. In the far zone the spectral–angular distribution of the emitted photons is obtained by using the well-known relation involving the Fourier transform of the retarded current [25]:

$$\frac{dN_i}{dv\, d\Omega} = \alpha v \left| \int dt \underline{n} \times (\underline{n} \times \underline{\beta}_i(t)) e^{i\omega(t - \underline{n}\cdot \underline{r}_i(t)/c)} \right|^2 \tag{1}$$

where $\underline{n}$ is the unit vector in the scattered direction (i.e. the direction of the observer), $\underline{\beta}_i(t)$ is the normalized velocity of the i-th electron, $\underline{r}_i(t)$ its position, $\alpha = 1/137$ is the fine structure constant and cgs units are used throughout. An analytic description of the electron trajectory is possible only in the case of flat-top laser pulses when transverse ponderomotive forces are negligible. For long pulses and small angles, the paraxial approximation is valid when $\sigma_z \gg \lambda_0$ and $|\vartheta_i| < 2w_0(\underline{\beta}_i)_z/\sigma_z$ ($\lambda_0 = c/\nu_0$ is the wavelength, σ_z the longitudinal r.m.s. dimensions, w_0 the waist diameter of the laser and ϑ_i is the polar angle of the i-th electron velocity), yields useful relations for the scattered radiation distribution [18] which are strictly valid for a flat-top laser profile and when transverse ponderomotive forces can be neglected. A generalization to non-flat top pulses (as in the case of ELI's settings) can be made by slicing the laser pulse in a sequence of sub-pulses of time duration $1/\nu_0 \ll T_s \ll \sigma_z/c$, in which the amplitude variation is negligible, and by solving the motion of the particles in each slice. The distribution of the scattered photons distribution of the s-th flat-top sub-pulse:

$$\left[\frac{dN_i}{dv\, d\Omega}\right]_s = \alpha(|V_{\theta,s}|^2 + |V_{\phi,s}|^2) \tag{2}$$

can be then generalized to the whole pulse by combining all contributions:

$$\frac{dN_i}{dv\, d\Omega} = \alpha(|V_\theta|^2 + |V_\phi|^2)$$

where $V_\theta = \sum_s V_{\theta,s}, V_\phi = \sum_s V_{\phi,s}$, and, in each slice, the terms $V_{\theta,s}$ and $V_{\phi,s}$ are computed according to Eq. (27) in Ref. [18]:

$$V_{\theta,s} = T_s \mathrm{sinc}\left(\frac{\Delta\omega_n T_s}{2}\right) e^{i\phi_s} \sum C_{\theta,s} \tag{3}$$

$$V_{\phi,s} = T_s \mathrm{sinc}\left(\frac{\Delta\omega_n T_s}{2}\right) e^{i\,\phi_s} \sum_n C_{\phi,s}. \tag{4}$$

In Eqs. (3) and (4) $\mathrm{sinc}(x) = \sin(x)/x$, $\Delta\omega_n = (\omega - n\omega_0)$, ϕ_s is the phase of the central oscillation in the slice and $C_{\theta,s}$, $C_{\phi,s}$ are complex terms involving Bessel J functions (see Eqs. (31) and (32) in Ref. [18]) in the paraxial limit. A sum over the harmonic number n accounts for the nonlinear effects. In the absence of correlation between the electrons, and in the moderate nonlinear regime, the generalization to an electron beam can be made by summing over the whole beam the contribution by the single electrons. Eqs. (3) and (4) generalize the computation of the scattered radiation in the linear and nonlinear regime reported in Ref. [18] to non-flat-top laser pulses that eventually diffract while interacting with the electron bunch. The use of the principle of the slicing for estimating analytically the contributions of the single particles is at the basis of the semi-analytic TSST (Thomson

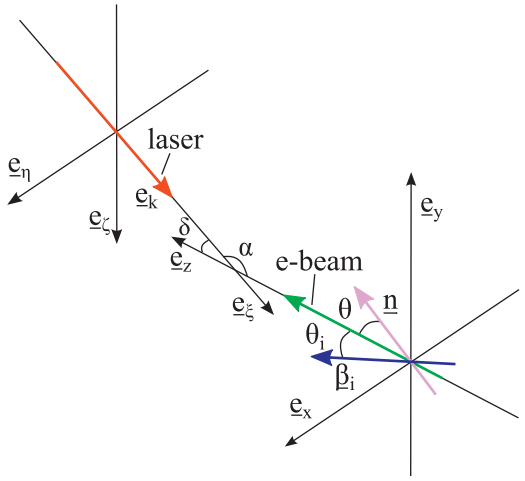

Fig. 1. Geometry of the laser–electron interaction. $\underline{e}_k$ is the unit vector of the laser wave vector, $\underline{\beta}_i$ is the electron normalized velocity, $\underline{n}$ is the scattered radiation direction, $\alpha=\pi-\delta$ is the angle between $\underline{e}_k$ and the axis of the electron beam $\langle\underline{\beta}_i\rangle=\underline{e}_z$, θ the angle between the electron beam axis and $\underline{n}$, and θ_i the angle between the i-th electron velocity $\underline{\beta}_i$ and the beam axis.

scattering simulation tools) code and turns out to be an accurate and fast procedure for radiation computation.

2.2. Beam interaction

As regards the laser system adopted, a Gaussian pulse has been supposed, with the normalized electric field A_L given by the expression:

$$A_L=\frac{E_L e^{-(\xi^2+\eta^2)/2\sigma_t^2(1+\varsigma^2/Z_R^2)-(\varsigma-ct\,\cos\,\alpha)^2/2\sigma_z^2+i\phi}}{h\overline{\nu}_0(2\pi)^{3/2}\sigma_t^2\sigma_z\sqrt{\left(1+\frac{z^2}{Z_R^2}\right)}}$$

$$\phi=\frac{\xi^2+\eta^2}{2\sigma_t^2\left(\frac{Z_R}{\varsigma}+\frac{\varsigma}{Z_R}\right)}-\mathrm{artg}\left(\frac{\varsigma}{Z_R}\right)$$

where ξ, η, ς are proper coordinates of the laser beam, connected with the laboratory frame by

$$\xi=x$$

$$\eta=y\,\cos\,\alpha-z\,\sin\,\alpha$$

$$\varsigma=y\,\sin\,\alpha+z\,\cos\,\alpha$$

with the geometry represented in Fig. 1.

Moreover, E_L is the maximum energy delivered by the laser, Z_R is the Rayleigh length, and σ_t the transverse r.m.s. dimensions of the laser field profiles.

The geometry of the interaction is described in Fig. 1. The axis of the electron beam $\langle\underline{\beta}_i\rangle$ coincides with the $\underline{e}_z$, and the laser beam wave vector forms an angle α with $\underline{e}_z$.

3. The quantum model

3.1. Compton cross-section

The Compton model permits to evaluate the final condition of the electron–photon system after the scattering in all those conditions where the recoil of the electron cannot be disregarded. From the momentum and energy conservation laws it follows that the electrons present, after the interaction, a diminished Lorentz factor given by

$$\gamma=\gamma_0-\frac{h}{mc^2}(\nu_p-\nu_0) \tag{5}$$

or

$$\gamma=\sqrt{1+\frac{\left(m\gamma_0 c\underline{\beta}_0+\frac{h\nu_0}{c}\underline{e}_k-\frac{h\nu_p}{c}\underline{n}\right)^2}{m^2c^2}}$$

where

$$\nu_p=\nu_0\frac{1-\underline{e}_k\cdot\underline{\beta}_0}{1-\underline{n}\cdot\underline{\beta}_0+\frac{h\nu_0}{mc^2\gamma_0}(1-\underline{n}\cdot\underline{e}_k)} \tag{6}$$

is the Compton frequency of the scattered photon. In these formulas, the index 0 refers to the coordinates before the scattering, $\underline{n}$ is the direction of the scattered photon and $\underline{e}_k$ is the unit vector of the direction of the incident photon of the laser.

A very useful expression is given by the wavelength:

$$\lambda_p=\lambda_0\frac{1-\underline{n}\cdot\underline{\beta}_0}{1-\underline{e}_k\cdot\underline{\beta}_0}+\frac{h}{mc\gamma_0}\frac{1-\underline{n}\cdot\underline{e}_k}{1-\underline{e}_k\cdot\underline{\beta}_0} \tag{7}$$

where the classic and quantum contributions appear clearly separated.

The electron velocity changes consequently as

$$\underline{\beta}=\underline{\beta}_0-\frac{h\nu_0}{mc^2\gamma_0}\frac{\left(1-\frac{\nu_p}{\nu_0}\right)\underline{\beta}_0+\underline{e}_z+\frac{\nu_p}{\nu_0}\underline{n}}{1+\frac{h\nu_0}{mc^2\gamma_0}\left(1-\frac{\nu_p}{\nu_0}\right)}. \tag{8}$$

From Eq. (8), the final velocity distribution of the electron beam can be reconstructed from the initial one and from the frequency and angular distribution of the photons. The photon–electron scattering is described by a cross-section deduced in the rest electron frame by Klein and Nishina [28,36], and revisited in Refs. [37,29,30,26].

The starting point is the Dirac equation:

$$i\hbar\frac{\partial\psi}{\partial t}=\hat{H}\psi$$

with

$$\hat{H}=\hat{H}_0+\hat{H}_{int}$$

where ψ is the wave function, and $\hat{H}$ the Hamiltonian formed by the unperturbed $\hat{H}_0$ and the interaction part $\hat{H}_{int}$.

Denoting with primes the quantities in the electron rest frame, the operator $\hat{H}_{int}$ contains the quantum radiation field:

$$\hat{\underline{A}}=c\underline{e}_0\sqrt{\frac{\hbar}{\nu_0'}}(e^{i(\underline{k}_0'\cdot\underline{r}'-2\pi\nu_0't')}\hat{a}_0+e^{-i(\underline{k}_0'\cdot\underline{r}'-2\pi\nu_0't')}\hat{a}_0^\dagger)$$
$$+c\underline{e}_p\sqrt{\frac{\hbar}{\nu_p'}}(e^{i(\underline{k}_p'\cdot\underline{r}'-2\pi\nu_p't')}\hat{a}+e^{-i(\underline{k}_p'\cdot\underline{r}'-2\pi\nu_p't')}\hat{a}^\dagger)$$

where $\hat{a}_0(\hat{a}_0^\dagger)$ and $\hat{a}(\hat{a}^\dagger)$ are creation (annihilation) operators and $\underline{e}_0$, $\underline{e}_p$ the polarization vectors relevant respectively to the incident and scattered photons. The linear transition probability is given by

$$w_{n,m}=\frac{2\pi}{\hbar}\rho\left|\sum_{n'}\frac{H_{m,n'}H_{n',n}}{E_m-E_n}\right|^2$$

with ρ the density of the states with energy E_m, and $H_{n,m'}$ and $H_{n',n}$ the interaction matrix elements projected on the common states given by the product of the spin states, the momentum and the radiation eigenfunctions. In the electron reference frame the differential transition probability $dw_{n,m}/d\Omega$ turns out to be

$$\frac{dw_{n,m}}{d\Omega}=c\frac{r_0^2}{4}\frac{\nu_p'^2}{\nu_0'^2}\left[4(\underline{e}_p'\cdot\underline{e}_0')^2+\frac{h\Delta\nu'}{mc^2}(1-\underline{n}'\cdot\underline{e}_k')\right]$$

and the cross-section

$$\left(\frac{d\sigma}{d\Omega}\right)' = \frac{r_0^2}{4}\frac{v_p'^2}{v_0'^2}\left[4(\underline{e}_p'\cdot\underline{e}_0')^2+\frac{v_0'}{v_p'}+\frac{v_p'}{v_0'}\right]$$

with $\underline{e}_0'$ and $\underline{e}_p'$ the photon polarizations before and after the scattering. In the laboratory reference frame, the differential Compton cross-section $d\sigma/d\Omega$ can be deduced by Lorentz transforming frequencies, polarizations and integration element over the solid angle according to the expressions:

$$v_p' = v_p\gamma_0(1-\underline{\beta}_0\cdot\underline{n})$$

$$v_0' = v_0\gamma_0(1-\underline{\beta}_0\cdot\underline{e}_k)$$

$$\underline{e}_0' = \underline{e}_0(1-\underline{\beta}_0\cdot\underline{e}_k)+\underline{\beta}_0\cdot\underline{e}_0\left(\underline{e}_k-\frac{\gamma_0}{\gamma_0+1}\underline{\beta}_0\right)$$

$$\underline{e}_p' = \underline{e}_p(1-\underline{\beta}_0\cdot\underline{n})+\underline{\beta}_0\cdot\underline{e}_p\left(\underline{n}-\frac{\gamma_0}{\gamma_0+1}\underline{\beta}_0\right)$$

$$d\Omega' = \frac{d\Omega}{\gamma_0^2(1-\underline{\beta}_0\cdot\underline{e}_k)^2}$$

obtaining

$$\left(\frac{d\sigma}{d\Omega}\right) = \frac{r_0^2X}{2\gamma_0^2(1-\underline{\beta}_0\cdot\underline{n})^2}\left(\frac{v_p}{v_0}\right)^2$$

with

$$X = \frac{v_0}{v_p}\frac{1-\underline{\beta}_0\cdot\underline{e}_k}{1-\underline{\beta}_0\cdot\underline{n}}+\frac{v_p}{v_0}\frac{1-\underline{\beta}_0\cdot\underline{n}}{1-\underline{\beta}_0\cdot\underline{e}_k}+\left(\underline{e}_0\cdot\underline{e}_p-\frac{c(\underline{\beta}_0\cdot\underline{e}_p)(\underline{e}_0\cdot\underline{p})}{hv_p(1-\underline{\beta}_0\cdot\underline{n})}+\frac{c(\underline{\beta}_0\cdot\underline{e}_0)(\underline{e}_p\cdot\underline{p})}{hv_0(1-\underline{\beta}_0\cdot\underline{e}_k)}\right)^2. \tag{9}$$

Finally, for the double differential cross-section we obtain

$$\frac{d^2\sigma}{dvd\Omega} = \frac{r_0^2X}{2\gamma_0^2(1-\underline{\beta}_0\cdot\underline{e}_k)^2}\left(\frac{v_p}{v_0}\right)^2 \delta\left(v_p-v_0\frac{1-\underline{e}_k\cdot\underline{\beta}_0}{1-\underline{n}\cdot\underline{\beta}_0+\frac{hv_0}{mc^2\gamma_0}(1-\underline{n}\cdot\underline{e}_k)}\right) \tag{10}$$

where the factor X, after averaging over the polarizations of the photons, becomes

$$X = \frac{v_0}{v_p}\frac{1-\underline{\beta}_0\cdot\underline{e}_k}{1-\underline{\beta}_0\cdot\underline{n}}+\frac{v_p}{v_0}\frac{1-\underline{\beta}_0\cdot\underline{n}}{1-\underline{\beta}_0\cdot\underline{e}_k}-1 +\left(1+\frac{mc^2}{hv_p\gamma_0}\frac{1}{1-\underline{\beta}_0\cdot\underline{n}}-\frac{mc^2}{hv_0\gamma_0}\frac{1}{(1-\underline{\beta}_0\cdot\underline{e}_k)}\right)^2. \tag{11}$$

Another delta function $\delta(mc(\underline{\beta}_0\gamma_0-\underline{\beta}\gamma)/h-(v_0\underline{e}_k-v_p\underline{n})/c)$ multiplies the cross-section and guarantees the conservation of the total momentum between the initial and the final configuration.

3.2. Beam interaction

We carry out the calculations with the same electron beam density as used in the classical scheme.

As regards the laser system, the same Gaussian pulse as the classical case has been supposed, with the photon density represented by modulus squared of the laser electric field:

$$\frac{dN_L}{d\underline{x}_0d\underline{k}_0} = \frac{E_LF(\underline{k}_0)}{h\overline{v}_0\pi^{3/2}\sigma_t^2\sigma_z\sqrt{\left(1+\frac{\zeta^2}{Z_R^2}\right)}}e^{-(\xi^2+\eta^2)/\sigma_t^2(1+z^2/Z_R^2)-(\varsigma-ct\ \cos\ \alpha)^2/\sigma_z}$$

where $\underline{x}_0$ and $\underline{k}_0$ are laser photon coordinates and momenta, Z_R is the Rayleigh length, E_L is the maximum energy delivered by the laser, $F(\underline{k}_0)$ the dependence on the photon momenta, σ_t and σ_z the transverse and longitudinal r.m.s. dimensions of the laser field profiles and $\overline{v}_0$ the central frequency value of the laser spectrum.

The number of emitted photons for frequency v and solid angle Ω units can be evaluated in the laboratory frame as

$$\frac{dN}{dv\,d\Omega} = h\int\frac{d\sigma}{dvd\Omega}\frac{dN_e}{d\underline{x}\,d\underline{p}}\frac{dN_L}{d\underline{x}_0\,d\underline{k}_0}d\underline{x}\,d\underline{p}\,d\underline{k}_0(1-\underline{\beta}_0\cdot\underline{e}_k)c\,dt. \tag{12}$$

The distribution of the electrons can be represented, in turn, by a sum of delta functions:

$$\frac{dN_e}{d\underline{x}d\underline{p}} = \sum_i\delta(\underline{x}-\underline{x}_i(t))\delta(\underline{p}-\underline{p}_i(t)) \tag{13}$$

with $\underline{x}_i(t)$ and $\underline{p}_i(t)$ coordinates of the i-th electron and the index i runs over all electrons. Once that Eq. (13) is inserted in Eq. (12), the number of emitted photons is

$$\frac{dN}{dv\,d\Omega} = h\sum_i\int\frac{d\sigma}{dv\,d\Omega}\frac{dN_L}{d\underline{x}_0d\underline{k}_0}(1-\underline{\beta}_0\cdot\underline{e}_k) \delta(\underline{x}-\underline{x}_i(t))\delta(\underline{p}-\underline{p}_i(t))\,d\underline{x}\,d\underline{p}\,d\underline{k}_0c\,dt \tag{14}$$

and the delta functions permit to solve the integrals in $d\underline{x}$ and $d\underline{p}$. Since the cross-section depends only on the electron momenta which are constant in time while the photon distribution depends on coordinates, one has

$$\frac{dN}{dv\,d\Omega} = h\sum_i\int\left[\frac{d\sigma}{dv\,d\Omega}\right]_{\underline{p}=\underline{p}_i} \left[\frac{dN_L}{d\underline{x}_0d\underline{k}_0}\right]_{\underline{x}=\underline{x}_i(t)}(1-\underline{\beta}_0\cdot\underline{e}_k)d\underline{k}_0c\,dt. \tag{15}$$

The distribution of the laser photons can be evaluated from the shape of the potential vector of the laser. We assume a simplified photon distribution depending only on the frequency f:

$$F(\underline{k}_0)d\underline{k}_0 = A_{Lv}(f)\,df = \frac{1}{\sqrt{\pi}\sigma_v}e^{-(f-\overline{v}_0)^2/\sigma_v^2}$$

where diffraction and curvature of the phase surfaces of the laser are disregarded with the assumption of an infinite Rayleigh length.

The df integral can be solved by using the delta function $\delta((mc^2/h)(\gamma-\gamma_0)+(v_p-f))=\delta(g(v_p,f))$:

$$\frac{dN}{dv\,d\Omega} = ch\int df\sum_i\left[\frac{d\sigma}{dv\,d\Omega}\right]_{\underline{p}=\underline{p}_i} A_{Lv}(f)(1-\underline{\beta}_0\cdot\underline{e}_k)\int[A_L]_{\underline{x}=\underline{x}_i(t)}\,dt. \tag{16}$$

According to the linear hypothesis, the unperturbed electron orbits can be assumed as

$$\underline{x}_i(t) = \underline{x}_{0i}+c\underline{\beta}_{0i}t \tag{17}$$

$$\underline{p}_i(t) = \underline{p}_{0i} \tag{18}$$

and the time integral evaluated analytically, giving

$$\frac{dN}{dv\,d\Omega} = \frac{E_L}{\overline{v}_0\pi^2\sigma_t\sigma_v}\int df\sum_i\left[\frac{d\sigma}{dv\,d\Omega}\right]_{\underline{p}_i} \times\delta(g(v_p,f))e^{-(f-\overline{v}_0)^2/\sigma_v^2}(1-\underline{\beta}_0\cdot\underline{e}_k)\times\frac{e^{\Psi(\underline{x}_{0i},\underline{\beta}_{0,i})}}{\sqrt{\sigma_z^2(\beta_{0ix}^2+\beta_{0iy}^2)+\sigma_t^2(1+\beta_{0iz})^2}}$$

with

$$f(v_p,f) = \delta\left(\frac{mc^2}{h}(\gamma-\gamma_0)+(v_p-f)\right) = \frac{\delta(f-v_0)}{\left|\frac{dg(v_p,f)}{df}\right|_{f=v_0}}$$

and

$$\left|\frac{dg(v_p,f)}{df}\right|_{f=v_0} = \frac{\left[(1-\underline{\beta}_0\cdot\underline{e}_k)-\frac{h}{m_0c^2\gamma_0}v_p(1-\underline{n}\cdot\underline{e}_k)\right]^2}{(1-\underline{n}\cdot\underline{\beta}_0)(1-\underline{\beta}_0\cdot\underline{e}_k)}$$

$$\Psi(\underline{x}_{0i},\underline{\beta}_{0,i}) = -\frac{x_{0i}^2+y_{0i}^2}{\sigma_t^2}-\frac{z_{0i}^2}{\sigma_z^2}+\frac{\left[\frac{(x_{0i}\beta_{0ix}+y_{0i}\beta_{0iy}}{\sigma_t^2}+\frac{z_{0i}(1-\beta_{0iz}\cos\alpha)}{\sigma_z^2}\right]^2}{2\left[\frac{\beta_{0ix}^2+\beta_{0iy}^2}{\sigma_t^2}+\frac{(1-\beta_{0iz}\cos\alpha)^2}{\sigma_z^2}\right]}.$$

Finally, we get

$$\frac{dN}{dv\,d\Omega} = \frac{E_L(1-\underline{\beta}_0\cdot\underline{e}_k)e^{\Psi(\underline{x}_{0i},\underline{\beta}_{0,i})}}{\overline{v}_0(2\pi)^{5/2}\sigma_t\sigma_v}\times\frac{\left[\sum_i\left[\frac{d\sigma}{dv\,d\Omega}\right]_{\underline{p}_i}\frac{e^{-(f-\overline{v}_0)^2/2\sigma_v^2}}{\left|\frac{dg(v_p,f_L)}{df}\right|}\right]_{f=v_0}}{\sqrt{\sigma_z^2(\beta_{0ix}^2+\beta_{0iy}^2)+\sigma_t^2(1+\beta_{0iz})^2}}$$

with

$$v_0 = v_p\frac{1-\underline{n}\cdot\underline{\beta}_0}{1-\underline{e}_k\cdot\underline{\beta}_0-\frac{hv_p}{mc^2\gamma_0}(1+\cos\theta)}.$$

4. Scaling laws and numerical data

Quantum effects can be weighted from the Compton formula, Eq. (7). A first regime, almost completely classical, occurs when

$$\lambda_0(1-\beta_0\cos(\theta+\theta_i)) \gg \frac{h}{mc\gamma_0}(1+\cos(\alpha+\theta_i))$$

that, for θ,θ_i and α much less than 1 can be written as

$$\lambda_0\left(\frac{1}{4\gamma_0^2}+\frac{\beta_0(\theta+\theta_i)^2}{2}\right) \gg \frac{h}{mc\gamma_0}\left(2+\frac{(\alpha+\theta_i)^2}{2}\right).$$

This is the usual Thomson classical regime, valid if $\gamma < mc^2/8hv_0$ and where the shift of the frequency is due only to Doppler effect. Acceptance and emittance effects extend the validity range of this regime.

If the incident radiation is a laser pulse with energy hv_0 ranging between 0.1 eV (CO_2 laser) and 10 eV (harmonics of the Ti:sapphire laser), the Thomson regime can protract up to electron beam energy of the order of several GeV. But if the relative bandwidth of the emitted radiation $\Delta v_p/v_p$ is required to be very thin by the particular foreseen application, the red shift of wavelength due to quantum effects must be taken into account already when $8\gamma hv_0/mc^2 \sim \Delta v_p/v_p$. If for instance $\Delta v_p/v_p \sim 10^{-3}$ the quantum shift on frequency begins to manifest at $\gamma \approx 100$.

If, however, the incident radiation has a very high frequency (in the range of UV, X or γ rays), the quantum recoil is always important, and, if $hv_0 > mc^2\gamma$, the energy of the emitted photon equals the energy of the electron $hv_p \approx mc^2\gamma_0$.

The quantum model has been applied to the electron beams whose parameters are summarized in Table 1 for typical cases of ELI, obtained by accelerating the electron beam in a high-brightness C-band linac driven by a S-band photoinjector [23].

As laser system we have hypothesized the second harmonics of a Nd:YLF laser ($\lambda_0 = 523{,}5$ nm), with an energy of 1 J, a temporal rms duration of 4 ps and a waist diameter of 35 μm. The interaction is supposed head-to-head, with the angle δ, defined in Fig. 1, null. In Fig. 2 we have compared the total number of photons (a) and relative bandwidth (b) vs the rms acceptance angle θ_{rms} (μrad) obtained by three numerical codes based on different models: CAIN (blue squares), which is a well-known quantum Monte Carlo code [31,32] bench-marked for Compton sources in Ref. [17], a semi-analytical quantum code based on the linear Compton model described previously (red squares) and the upgraded version of the classical nonlinear code TSST (black squares) [18] in the case of the electron beam parameters of beam (A).

Table 1
Main parameters of electron, laser and radiation beams for the ELI project.

Quantity	Beam A	Beam B
Charge Q (C)	0.25×10^{-9}	0.25×10^{-9}
Energy E (MeV)	360	720
Energy spread δE (MeV)	0.234	0.36
Horizontal emittance (mm mrad)	0.65	0.5
Vertical emittance (mm mrad)	0.6	0.5
Laser wavelength (μm)	0.523	0.523
Laser energy E_L (J)	1	1
Laser rms time duration (ps)	4	4
Laser waist (μm)	35	35
Photon energy (MeV)	4.9	18.8
Quantum red shift (keV)	67	533

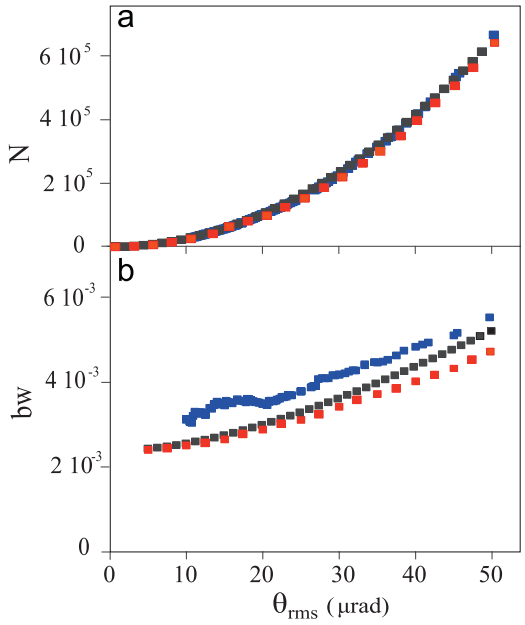

Fig. 2. Comparison of the total number of photons N (a) and relative bandwidth bw (b) vs the rms acceptance angle θ_{rms} (μrad) of the data obtained by the CAIN code (blue), the Compton model (red) and the classical nonlinear theory TSST (black). The electron beam used is the working point A (Table 1). The total number of photons is almost exactly the same. As regards the bandwidth, differences within 20% were found. (For interpretation of the references to color in this figure caption, the reader is referred to the web version of this article.)

While for the total number of photons the agreement presented by the three different models appears striking, differences within 20%, are shown by the values of the bandwidth.

A photon number of order 10^5 for a bandwidth of few 10^{-3} is obtained in a cone of acceptance θ_{rms} of order 10 μrad.

In particular, for a bandwidth at the nominal value 3×10^{-3}, 1.5×10^5 photon are collected in about 25 μrad.

The spectra produced by the three codes are presented in Fig. 3 for the same beam of Fig. 2 and $\theta_{rms} = 25$ μrad. We can see here that the differences on the bandwidth values, shown in Fig. 2(b), have to be attributed to the discrepancies in the tails, the rms evaluation being very sensible to them.

As can be seen, the quantum effects introduce a redshift in energy, that, in the present regime, can be quantified in the value $h\Delta v \sim 3.1\times10^{-5}\gamma^3(hv_0)^2 = 67$ keV. The classical calculations give therefore a larger value of the mean frequency, while the shape, the peak and the width of the spectra are very similar for all cases.

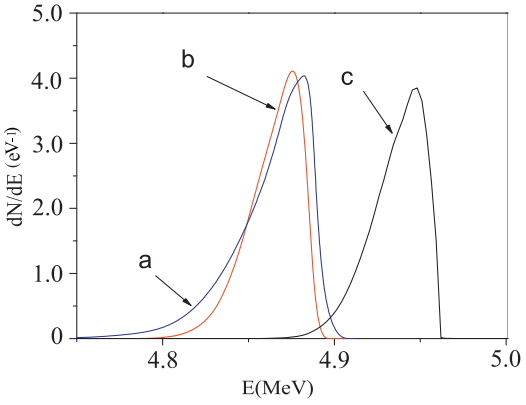

Fig. 3. Spectra of the γ rays. (a) CAIN. (b) Quantum model. (c) Classical treatment in the case of beam (A) and for the laser parameter of Table 1 and interaction angle $\alpha=\pi$, rms acceptance angle $\theta_{rms}=25$ μrad.

A simple model based on the luminosity concept permits to deduce a very useful scaling law for the total number of photons emitted in a cone of rms emi-angle θ_{rms}. Assuming, in fact, an electron beam with circular transverse section of radius σ_x, the photon number for a single shot scales as

$$N=\frac{\sigma_{Th}}{\pi\sigma_x^2}N_eN_L\Psi^2=\frac{0.83\times10^9E_LQ\Psi^2}{h\nu_L\sigma_x^2} \tag{19}$$

where $\sigma_{Th}=0.67$ barn is the Thomson cross-section, $\Psi=\gamma_0\theta_{rms}$ is the acceptance of the system, N_e the total number of electrons in the beam and N_L the total number of photons in the laser pulse, and in the right hand term the energy of the laser is in Joule, the charge Q in pC, the factors $h\nu$ in eV and the lengths in μm. Inserting the data of Table 1, and $\sigma_x=13.5$ μm, Eq. (19) fits very accurately the results of Fig. 3. The bandwidth, deduced from the Compton relation (7), scales with the quadratic sum of contributes due respectively to the acceptance Ψ, to the normalized emittance ϵ_n, to the laser natural bandwidth, diffraction and temporal profile, similar to the corresponding classical terms:

$$\left[\frac{\Delta\nu_p}{\nu_P}\right]_{\Psi}\approx\Psi^2$$

$$\left[\frac{\Delta\nu_p}{\nu_P}\right]_{\epsilon}\approx\left[\frac{\epsilon_n}{\sigma_x}\right]^2$$

$$\left[\frac{\Delta\nu_p}{\nu_P}\right]_{\Delta\nu_0}\approx\frac{\Delta\nu_0}{\nu_0}$$

$$\left[\frac{\Delta\nu_p}{\nu_P}\right]_{d}\approx\left[\frac{M^2\lambda_L}{2\pi w_0}\right]^2$$

$$\left[\frac{\Delta\nu_p}{\nu_P}\right]_{\sigma_z}\approx\left[\frac{a_0^2/3}{1+a_0^2/2}\right].$$

The term due to the energy spread of the beam $\Delta\gamma$ has, however, a different expression, due to the presence of the quantum frequency shift. In fact

$$\left[\frac{\Delta\nu_p}{\nu_P}\right]_{\Delta\gamma}\approx\frac{2\Delta\gamma}{\gamma}\left[1-\frac{2h\nu_0\gamma}{mc^2}\frac{1}{1+\frac{4h\nu_0}{mc^2}\gamma}+\Upsilon(\theta,\theta_i)\right]$$

with

$$\Upsilon=-\frac{1}{2}\left(1+\frac{1}{\left(1+\frac{4h\nu_0}{mc^2}\gamma\right)^2}\right)\Theta^2+\frac{2h\nu_0\gamma}{mc^2}\frac{\Theta}{1+\frac{4h\nu_0}{mc^2}\gamma}^2\frac{h\nu_0}{mc^2}+\frac{\epsilon_n^2}{2\gamma\left(1+\frac{4h\nu_0}{mc^2}\gamma\right)^2}$$

and

$$\Theta^2=(\gamma\theta_i+\gamma\theta)^2$$

shows that quantum effects contribute to frozen the beam and to decrease the bandwidth broadening from $2\Delta\gamma/\gamma$ to $\Delta\gamma/\gamma$, provided that acceptance $\gamma\theta$ and emittance $\gamma\theta_i$ terms are sub-dominant.

The relative bandwidth has the expression:

$$\frac{\Delta\nu_p}{\nu_P}\approx\sqrt{\Psi^4+\left[\frac{\epsilon_n}{\sigma_x}\right]^4+\left[\frac{\Delta\nu_p}{\nu_P}\right]_{\Delta\gamma}^2+\left[\frac{\Delta\nu_p}{\nu_P}\right]_L^2} \tag{20}$$

where in the last term all contributions of the laser are taken into account. Once the bandwidth has been fixed at the required value $[\Delta\nu_p/\nu_p]_r$ the corresponding acceptance is

$$\Psi_r^2\approx\sqrt{\left[\frac{\Delta\nu_p}{\nu_P}\right]_r^2-\left[\frac{\epsilon_n}{\sigma_x}\right]^4-\left[\frac{\Delta\nu_p}{\nu_P}\right]_{\Delta\gamma}^2-\left[\frac{\Delta\nu_p}{\nu_P}\right]_L^2} \tag{21}$$

and the spectral density in the bandwidth in a single shot defined as

$$S=\frac{N}{\Delta\nu_p/\nu_p}$$

turns out to be

$$S_r(\mathrm{eV}^{-1})=\frac{0.83\times10^9E_LQ\Psi^2}{h\nu_L\sigma_x^2}\frac{1}{\left[\frac{\Delta\nu_p}{\nu_p}\right]_r}. \tag{22}$$

Figs. 4 and 5 show the numerical optimization of the spectral density with respect the transverse dimension σ_x of the electron beam (triangles, left axis), obtained by changing the final focusing system, for the low and the high energy cases, together with the acceptance angle on the right. In the optimization the normalized emittance of the electron beam remains constant and both transverse size and transverse momenta of the electrons changes accordingly. As can be seen in the figures, the spectral density, once fixed the required bandwidth at the value $[\Delta\nu_p/\nu_p]_r=3\times10^{-3}$, shows a maximum for a value of σ_x. For beams characterized by high focusing, the term $[\Delta\nu_p/\nu_P]_\epsilon$ dominates in the bandwidth, thus limiting the collection of the photons to a small acceptance angle. Lower focusing decreases the transverse momenta of the electrons in the interaction region and permits to increase the acceptance. A further relaxation in the focusing leads to a low density beam with radius larger than the laser waist and to a diminishing spectral density. In our case the maximum value of photons $S_{r,max}=1.2\times10^8$ occurs for $\sigma_x(S_{r,max})=17$ μm for the lower energy beam, while $S_{r,max}=1.15\times10^9$ for $\sigma_x(S_{r,max})=16$ μm in the higher energy case. In Figs. 4 and 5, the validation of Eq. (22) (solid lines) is also shown. All these numbers

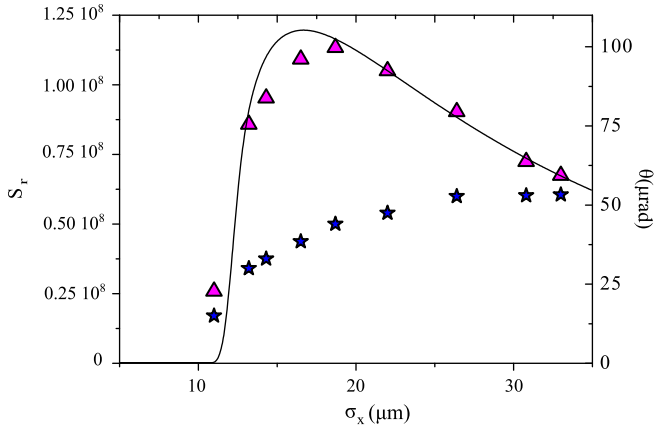

Fig. 4. Spectral density S_r (e V^{-1}) vs rms electron beam transverse dimension σ_x (μm, triangles, left axis) and corresponding acceptance angle (stars, right axis) in the case of beam A. The solid line is the plot of Eq. (22) for the same value.

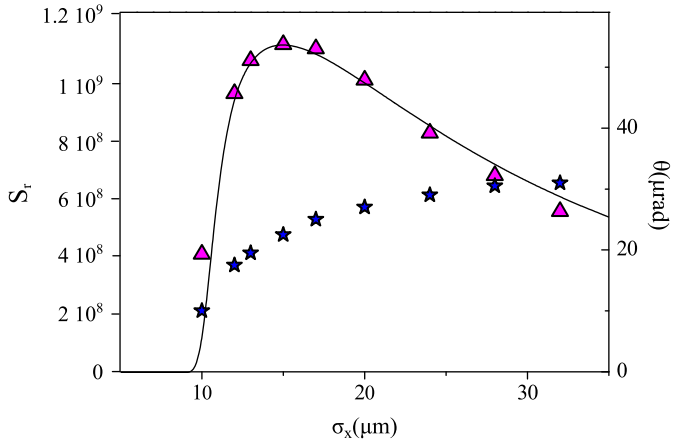

Fig. 5. Spectral density S_r (eV^{-1}) vs rms electron beam transverse dimension σ_x (μm, triangles, left axis) and corresponding acceptance angle (stars, right axis) in the case of beam B. The solid line is the plot of Eq. (22) for the same value.

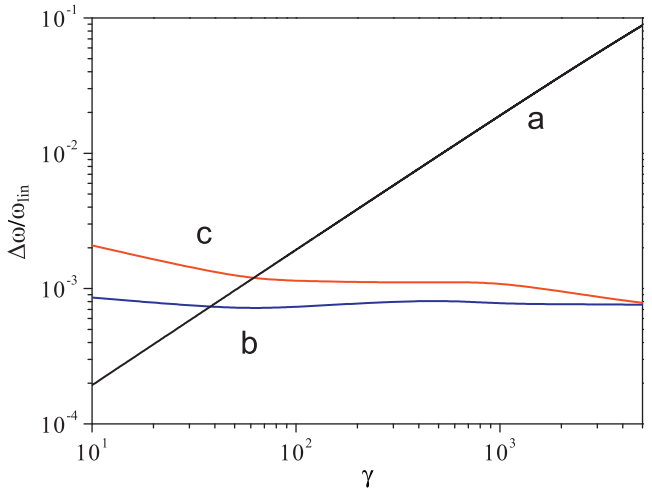

Fig. 6. Normalized frequency shift as function of γ. (a) Quantum model, (b) $a_0 = 0.03$ and (c) $a_0 = 0.3$.

represent the values obtained in a single shot. Another important parameter for the characterization of the γ-source is the spectral density per eV, that in previous the cases turns out to be 18 electrons per eV in the first case and 6 electron per eV in the second.

An upgrade of the photoinjector, now under study, permits the operation at 100 Hz, enhancing by an extra factor $F_{pj} = 10^2$ the photon number per eV and per second.

A system of recirculation of the laser pulse producing a train of 20–30 packets provides moreover a multiplication factor $F_r = 20-30$, that finally permits to increase the photon number per second in a bandwidth of 3×10^{-3} by an overall factor $F_{pj}F_r = 2-3 \times 10^3$. The spectral density of photons per r.s.m. bandwidth become respectively $2.4-3.6 \times 10^{11}$ ($3.6-5.4 \times 10^4$ per eV) for the low energy case, and $2.3-3.45 \times 10^{12}$ ($1.2-1.8 \times 10^4$ per eV) for the high energy case. Since this last device can introduce losses and limits therefore the laser energy, the previous values have to be intended as number of photons per eV per second and per Joule of laser energy and scaled accordingly with the effective laser energy.

As regards the nonlinear effects due to strong laser energy, we are carrying out an analysis based on the numerical solution of the trajectories of the electrons under a realistic laser profile and on their insertion in Eq. (1). The nonlinearity, in general, induces a series of distortions in the spectrum appearing in sequence with increasing laser energy: a shift in the spectrum towards lower energies, a broadening in the bandwidth, the rising of side bands, the growth of harmonics, the enhancement of the background, the superposition, shift and merging of all harmonics. In the case of the parameters of ELI, the only effect that appears is a weak shift of the frequency peak, which is however much lower than quantum shift. In Fig. 6 the nonlinear shift for the case $a_0 = 0.03$ (curve (b)) and $a_0 = 0.3$ (curve (c)) are compared with the quantum one (curve (a)). For the typical values of the ELI working points we have considered ($600 < \gamma < 1500$, $a_0 \approx 0.03$), the quantum shift exceeds by more than one order of magnitude the nonlinear one, and even an a_0 10 times larger do not change this order.

5. Conclusions

A study of the radiation generated by a γ source with parameters similar to those of ELI-NP is presented. The scheme adopted is based on the back-scattering between electrons produced by a linac and photons coming from an optical laser at the present status of art. The indicative values of the parameters of the electron beam have been deduced by start-to-end simulations that are presented in Ref. [23]. By the comparison of the results of three independent models (the classical nonlinear deterministic TSST code, a semi-analytical quantum linear one, and CAIN), we are able to conclude that (i) the quantum model in the range analyzed (electron energy about 300–700 MeV, laser wavelength ~ 500 nm) is important to determine the radiation frequency, whose shift with respect to the classical value scales as γ^3. (ii) The other characteristics of the radiation, as, for instance, the shape of the spectrum, the total number of photons, the bandwidth, are not substantially affected by quantum effects. (iii) Also classical nonlinear effects do not seem to play a significant role, due to the limited value of the laser energy (< 1 J), corresponding to values of the laser parameter $a_0 \sim 0.03$. (iv) Collective and microbunching effects on the electron beam, that could, in principle, lead the system to exponential gain and decrease the divergence of the radiation, would require prohibitive values of laser energy and must be completely excluded. (v) Finally, ambiguous mathematical procedures in the Klein–Nishina cross-section derivation (such as, for instance, the use of improper eigenfunctions and the occurrence of squared Dirac delta functions), should be eliminated by a rigorous revision.

Simple scaling laws, based on the concept of luminosity and validated by numerical simulations, provide an useful tool for the immediate dimensioning of the experiments.

At the nominal value of relative bandwidth 310^{-3} (a number suitable for beginning nuclear resonance fluorescence measurements), about 10 photons per eV can be collected per single interaction and per Joule of laser energy. Multi-bunch and laser recirculation techniques can increase this value up to $\gtrsim 10^4$, thus rendering this γ source interesting for future applications in nuclear fields.

References

[1] J. Miao, et al., Proceedings of the National Academy of Science of the United States 100 (2003) 110.
[2] H.N. Chapman, et al., Nature Physics 2 (2006) 839.
[3] I. Robinson, Physical Review Letters 87 (2001) 195505.
[4] M. Pfeifer, Nature 442 (2006) 63.
[5] D. Shapiro, et al., Proceedings of the National Academy of Science of the United States 102 (2005) 15343.
[6] K.J. Gaffney, H.N. Chapman, Science 316 (2007) 1444.
[7] M. Pfeifer, Nature 442 (2006) 63.
[8] T. Shintake, et al., Nature Photonics 2 (2008) 555.
[9] Z. Huang, et al., Physical Review Special Topics—Accelerators and Beams 13 (2010) 020703.

[10] L. Giannessi, et al., Physical Review Special Topics—Accelerators and Beams 14 (2011) 060712.
[11] W. Ackermann, et al., Nature Photonics 1 (2007) 336.
[12] J. Mauritsson, et al., Physical Review A 70 (2004) 021801. (R).
[13] M. Bech, O. Bunk, C. David, R. Ruth, J. Rifkin, R. Loewen, I. Feidenhans'l, F. Pfeier, Journal of Synchrotron Radiation 16 (2009) 43.
[14] M. Babzien, et al., Physical Review Letters 96 (2006) 054802.
[15] D.J. Gibson, F. Albert, S.G. Anderson, S.M. Betts, M.J. Messerly, H. Phan, V.A. Semenov, M. Shverdin, A.M. Tremaine, F. Hartemann, et al., Physical Review Special Topics—Accelerators and Beams 13 (2010) 070703.
[16] G. Priebe, et al., Laser and Particle Beams 26 (2008) 649.
[17] C. Sun, Y.K. Wu, Physical Review Special Topics—Accelerators and Beams 14 (2011) 044701.
[18] P. Tomassini, A. Giulietti, D. Giulietti, L. Gizzi, Applied Physics B 80 (2005) 419.
[19] P. Tomassini, et al., IEEE Transactions on Plasma Science 36 (2008) 1872.
[20] P. Oliva, A. Bacci, U. Bottigli, M. Carpinelli, P. Delogu, M. Ferrario, D. Giulietti, B. Golosio, V. Petrillo, L. Serafini, et al., Nuclear Instruments and Methods in Physics Research Section A 615 (2010) 93.
[21] L.A. Gizzi, A. Bacci, S. Betti, et al., European Physical Journal Special Topics 175 (2009) 3.
[22] M. Ferrario, et al., Physical Review Letters 104 (2010), ISSN 0031-9007.
[23] C. Vaccarezza, et al., in: Proceeding of the IPAC 2012 Conference, TUOBB01, 2012.
[24] F. Albert, F.V. Hartemann, S.G. Anderson, R.R. Cross, D.J. Gibson, J. Hall, R.A. Marsh, M. Messerly, S.S. Wu, C.W. Siders, et al., Physics of Plasmas 19 (2012) 056701.
[25] J. Jackson, Classical Electrodynamics, 2nd ed., John Wiley and Sons, New York, 1975.
[26] F. Hartemann, Nuclear Instruments and Method in Physics Research A 608 (2009) S1.
[27] F. Albert, S.G. Anderson, D.J. Gibson, C.A. Hagmann, M.S. Johnson, M. Messerly, V. Semenov, M.Y. Shverdin, B. Rusnak, A.M. Tremaine, et al., Physical Review Special Topics—Accelerators and Beams 13 (2010) 070704.
[28] O. Klein, Z. Nihina, Zeitschrift für Physik 52 (1929) 853.
[29] J. Jauch, F. Rohrlich, The Theory of Photons and Electrons, Addison Wesley, 1955.
[30] G. Bhatt, H. Grotch, E. Kazes, D. Owen, Physical Review A 28 (1983) 2195.
[31] K. Yokoya, KEK Report 85-96, October 1985.
[32] CAIN 〈http://www-acc-theory.kek.jp/members/cain〉, 1985.
[33] S. Ride, E. Esarey, M. Baine, Physical Review E 52 (1995) 5425.
[34] W. Brown, F. Hartemann, Physical Review Special Topics—Accelerators and Beams 7 (2004) 060703.
[35] W. Brown, S. Anderson, C. Barty, S. Betts, R. Booth, J. Crane, et al., Physical Review Special Topics—Accelerators and Beams 7 (2004) 060702.
[36] W. Heitler, The Quantum Theory of Radiation (The International Series of Monography in Physics), 1954.
[37] J. Stepanek, Nuclear Instruments and Method in Physics Research A 412 (1998) 174.